# Six hundred years of South American tree rings reveal an increase in severe hydroclimatic events since mid-20th century

Mariano S. Morales[a,b,1], Edward R. Cook[c], Jonathan Barichivich[d,e], Duncan A. Christie[e,f], Ricardo Villalba[a], Carlos LeQuesne[e], Ana M. Srur[a], M. Eugenia Ferrero[a], Álvaro González-Reyes[g], Fleur Couvreux[h], Vladimir Matskovsky[a,i], Juan C. Aravena[j], Antonio Lara[e,f], Ignacio A. Mundo[a,k], Facundo Rojas[a], María R. Prieto[a], Jason E. Smerdon[c], Lucas O. Bianchi[a,l], Mariano H. Masiokas[a], Rocio Urrutia-Jalabert[e,f,m], Milagros Rodriguez-Catón[a,c], Ariel A. Muñoz[f,n], Moises Rojas-Badilla[e], Claudio Alvarez[e], Lidio Lopez[a], Brian H. Luckman[o], David Lister[p], Ian Harris[p], Philip D. Jones[p], A. Park Williams[c], Gonzalo Velazquez[e], Diego Aliste[e,f], Isabella Aguilera-Betti[n,q], Eugenia Marcotti[a,r], Felipe Flores[e], Tomás Muñoz[e], Emilio Cuq[e], and José A. Boninsegna[a]

[a]Instituto Argentino de Nivología, Glaciología y Cs. Ambientales, Consejo Nacional de Investigaciones Científicas y Técnicas (CONICET), 5500 Mendoza, Argentina; [b]Laboratorio de Dendrocronología, Universidad Continental, 12003 Huancayo, Perú; [c]Lamont-Doherty Earth Observatory, Columbia University, Palisades, NY 10964-1000; [d]Laboratoire des Sciences du Climat et de l'Environnement, Institut Pierre Simon Laplace, CNRS/Commissariat à l'Energie Atomique/Université de Versailles Saint-Quentin-en-Yvelines, 91191 Gif sur Yvette, France; [e]Laboratorio de Dendrocronología y Cambio Global, Instituto de Conservación Biodiversidad y Territorio, Universidad Austral de Chile, Valdivia 5110566, Chile; [f]Center for Climate and Resilience Research (CR)$^2$, Santiago 8370415, Chile; [g]Hémera Centro de Observación de la Tierra, Escuela de Ingeniería Forestal, Facultad de Ciencias, Universidad Mayor, Huechuraba, Santiago 8580745, Chile; [h]Centre National de Recherches Météorologiques, Université de Toulouse Météo-France CNRS, Toulouse, 31057, France; [i]Institute of Geography, Russian Academy of Sciences, 119017 Moscow, Russia; [j]Centro de Investigación Gaia Antártica, Universidad de Magallanes, Punta Arenas 620-0000, Chile; [k]Facultad de Ciencias Exactas y Naturales, Universidad Nacional de Cuyo, M5502JMA Mendoza, Argentina; [l]Instituto de Investigaciones en Recursos Naturales, Agroecología y Desarrollo Rural, Universidad Nacional de Río Negro, Consejo Nacional de Investigaciones Científicas y Técnicas, 8400 San Carlos de Bariloche, Argentina; [m]Instituto Forestal (INFOR), 5090000 Valdivia, Chile; [n]Laboratorio de Dendrocronología y Estudios Ambientales, Instituto de Geografía, Pontificia Universidad Catolica de Valparaíso, Valparaíso 2374631, Chile; [o]Department of Geography, University of Western Ontario, London, ON N6A 3K7, Canadá; [p]Climatic Research Unit, University of East Anglia, Norwich NR4 7TJ, United Kingdom; [q]Centro Transdisciplinario de Estudios Ambientales y Desarrollo Humano Sostenible, Universidad Austral de Chile, Valdivia 5091000, Chile; and [r]Instituto de Ecorregiones Andinas–Consejo Nacional de Investigaciones Científicas y Técnicas–Universidad Nacional de Jujuy, 4600 Jujuy, Argentina

Edited by James C. Zachos, University of California, Santa Cruz, CA, and approved June 1, 2020 (received for review February 18, 2020)

**South American (SA) societies are highly vulnerable to droughts and pluvials, but lack of long-term climate observations severely limits our understanding of the global processes driving climatic variability in the region. The number and quality of SA climate-sensitive tree ring chronologies have significantly increased in recent decades, now providing a robust network of 286 records for characterizing hydroclimate variability since 1400 CE. We combine this network with a self-calibrated Palmer Drought Severity Index (scPDSI) dataset to derive the South American Drought Atlas (SADA) over the continent south of 12°S. The gridded annual reconstruction of austral summer scPDSI is the most spatially complete estimate of SA hydroclimate to date, and well matches past historical dry/wet events. Relating the SADA to the Australia–New Zealand Drought Atlas, sea surface temperatures and atmospheric pressure fields, we determine that the El Niño–Southern Oscillation (ENSO) and the Southern Annular Mode (SAM) are strongly associated with spatially extended droughts and pluvials over the SADA domain during the past several centuries. SADA also exhibits more extended severe droughts and extreme pluvials since the mid-20th century. Extensive droughts are consistent with the observed 20th-century trend toward positive SAM anomalies concomitant with the weakening of midlatitude Westerlies, while low-level moisture transport intensified by global warming has favored extreme rainfall across the subtropics. The SADA thus provides a long-term context for observed hydroclimatic changes and for 21st-century Intergovernmental Panel on Climate Change (IPCC) projections that suggest SA will experience more frequent/severe droughts and rainfall events as a consequence of increasing greenhouse gas emissions.**

drought atlas | palaeoclimate reconstruction | extreme hydroclimate events | South America hydroclimate | Southern Hemisphere climate modes

Productive economic and social activities in South America (SA) are heavily dependent on hydroclimate variability. Severe water shortages have occurred in central Chile and western Argentina during the drought years 1968 to 1969, 1976 to 1977, 1996 to 1997, and 2010 to 2019 due to a deficit in snow accumulation in the Andes. Farmers in western Argentina reported between 35% and 50% crop losses as a consequence of water supply reduction in 1968/69 (1). This specific event, known as the Great Drought of 1968, also had serious impacts in central Chile. Cereal and vegetable production dropped by 65%, irrigation areas contracted by 40%, and livestock numbers decreased by 45% across the country, leading to the loss of 225,000 agricultural jobs (2). Presently, this region is experiencing the most severe decadal drought identified during the last millennium (3). Socioeconomic disasters such as those associated with the 1968 drought highlight the acute vulnerability of SA to extreme droughts, motivating improved understanding of the occurrence, duration, and spatial extent of

Author contributions: M.S.M., E.R.C., J.B., D.A.C., R.V., C.L., B.H.L., and J.A.B. designed research; M.S.M. performed research; M.S.M., E.R.C., J.B., A.G.-R., F.C., and V.M. contributed new reagents/analytic tools; M.S.M., E.R.C., J.B., D.A.C., R.V., C.L., A.M.S., M.E.F., A.G.-R., F.C., V.M., F.R., M.R.P., J.E.S., L.O.B., M.H.M., A.A.M., M.R.-B., C.A., L.L., D.L., I.H., P.D.J., A.P.W., G.V., D.A., I.A.-B., E.M., F.F., T.M., and E.C. analyzed data; M.S.M. wrote the paper; E.R.C., J.B., D.A.C., R.V., C.L., A.M.S., M.E.F., A.G.-R., F.C., V.M., J.C.A., A.L., I.A.M., F.R., M.R.P., J.E.S., L.O.B., R.U.-J., M.R.-C., B.H.L., P.D.J., A.P.W., and J.A.B. reviewed and edited versions of the paper; R.V., D.A.C., C.L., M.E.F., J.C.A., A.L., I.A.M., M.H.M., R.U.-J., M.R.-C., A.A.M., M.R.-B., C.A., L.L., G.V., D.A., I.A.-B., F.F., T.M., E.C., and J.A.B. provided tree ring chronologies and interpretation; M.S.M., J.B., A.M.S., F.C., L.O.B., M.R.-C., and E.M., compiled the instrumental database; and D.L., I.H., and P.D.J. produced the gridded instrumental database.

The authors declare no competing interest.

This article is a PNAS Direct Submission.



Data deposition: Instrumental and reconstructed scPDSIs have been deposited at the Center for Climate and Resilience Research (CR)$^2$, http://www.cr2.cl/datos-dendro-sada/.

[1]To whom correspondence may be addressed. Email: mmorales@mendoza-conicet.gob.ar.

This article contains supporting information online at https://www.pnas.org/lookup/suppl/doi:10.1073/pnas.2002411117/-/DCSupplemental.

First published July 6, 2020.

## Significance

**The SADA is an annually-resolved hydroclimate atlas in South America that spans the continent south of 12°S from 1400 to 2000 CE. Based on 286 tree ring records and instrumentally-based estimates of soil moisture, the SADA complements six drought atlases worldwide filling a geographical gap in the Southern Hemisphere. Independently validated with historical records, SADA shows that the frequency of widespread severe droughts and extreme pluvials since the 1960s is unprecedented. Major hydroclimate events expressed in the SADA are associated with strong El Niño Southern Oscillation (ENSO) and Southern Annular Mode (SAM) anomalies. Coupled ENSO-SAM anomalies together with subtropical low-level jet intensification due to increasing greenhouse gas emissions may cause more extreme droughts and pluvials in South America during the 21st century.**

extreme hydroclimatic events. The steep Andean topography, in turn, induces larger spatial heterogeneity in the climate that is not captured by the few high-elevation climatic records available for the region. Therefore, climate forecasts and projections for the areas adjacent to the Andes present large uncertainties due to the limited capacity of global climate models to simulate processes at regional scales in mountainous regions (4).

In tropical latitudes, South American hydroclimate is dominated by the seasonal migration of the South American monsoon (5). In the extratropical Andes, the climate is influenced by latitudinal changes of the South Pacific storm tracks leading to a winter precipitation regime. The region to the east, in the rain shadow of the Andes, has a weaker seasonal cycle of rainfall but a summer maximum reflecting a larger influence of the Atlantic than the Pacific Ocean over this region (6). It has long been known that the El Niño–Southern Oscillation (ENSO), the Southern Annular Mode (SAM), and tropical Atlantic sea surface temperature (SST) variability play major roles in forcing SA hydroclimate over seasonal to multidecadal scales (5–7). ENSO in the tropical Pacific is the dominant driver of interannual climate variations with profound worldwide impacts through atmospheric teleconnections (8, 9), whereas SAM is the main forcing of climate variability from mid- to high latitudes in the Southern Hemisphere (SH) (10).

The persistently positive trend in the SAM over the last few decades, in part driven by stratospheric ozone depletion (11), has induced important hydroclimatic anomalies over SA, some of which are unprecedented in the instrumental period (12). Additionally, rising greenhouse gases have recently modulated changes in tropical–subtropical SST patterns over both the Pacific and Atlantic Oceans, causing a persistent, decade-long drought in the subtropical Andes (12). The drying trend along the western-central coast of SA during the past decades is also consistent with the expansion of the Hadley cell and the poleward shift of the westerlies (12–14). During cold ENSO phases,



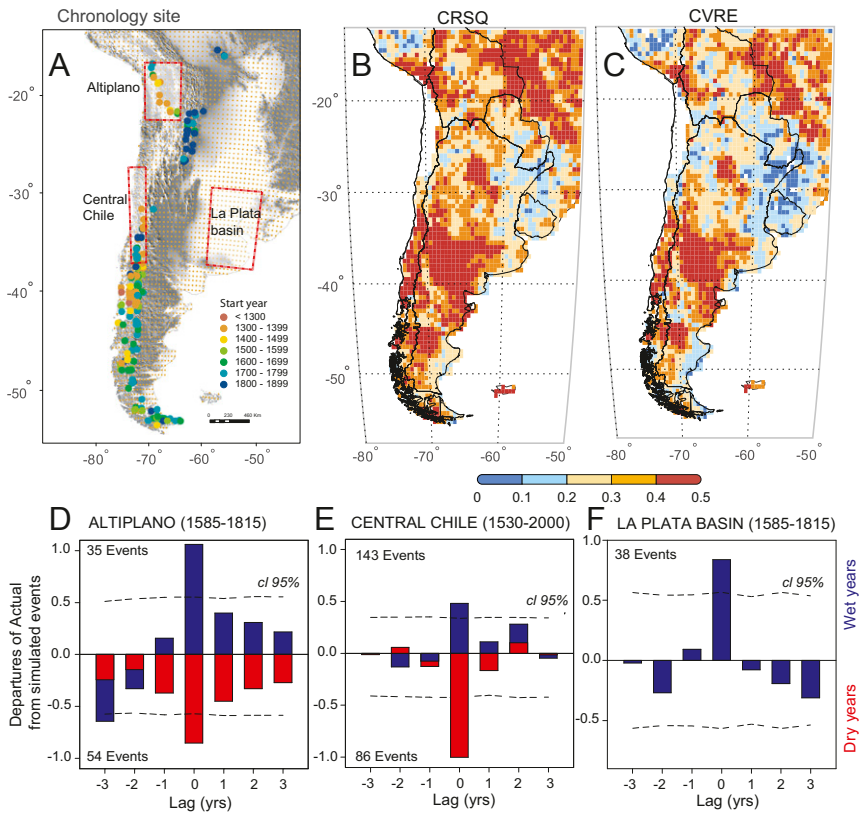


**Fig. 1.** SADA domain and verifications based on instrumental climate and historical documents. (*A*) Map of the DJF scPDSI target field (small orange dots mark grid-point centers) and the network of 286 tree ring chronologies used for reconstruction (circles colored to indicate start year). (*B*) Calibration-period regression coefficient of determination (CRSQ); the white region over northern Chile indicates where the reconstruction was not performed. (*C*) Calibration period leave-one-out cross-validation reduction of error (CVRE). (*D–F*) Superposed epoch analyses (SEAs) for reconstructed scPDSI (red rectangles in map) during the dry/wet events recorded by historical documents from (*D*) Potosí, Bolivia (1585 to 1807), (*E*) central Chile (1530 to 2000), and (*F*) Santa Fe city (1585 to 1815; La Plata basin). The red/blue bars represent scPDSI departure from normal conditions for a 9-y window ($t - 4$ to $t + 4$) based on 1,000 Monte Carlo simulations for the dry/wet historical events, respectively. The short dashed lines represent the 95% confidence limits.

the poleward shifts of the westerlies were enhanced by the concomitant SAM positive phase (15, 16). Hence, the expansion of the Hadley cell descending branch concurrent with the southward shift of the westerlies has increased the frequency of dry events in the subtropical Andes, the temperate and cold regions of SA (12, 13).

Despite all these alarming trends in SA's hydroclimate, the brevity of available instrumental climate records (usually less than 60 y) can only provide a limited view of extremes in natural hydroclimate variability. A long-term and large-scale perspective is necessary to document the historical range and sequence of hydroclimate variations in SA, their connections to large-scale climate modes and their interactions (e.g., ENSO and the SAM), and the impacts of external climate forcings. In many regions of SA, climate proxies such as tree rings, ice cores, sediments, speleothems, and historical archives have been used successfully to reconstruct hydroclimatic variations over centuries to millennia (17–19). However, the local geographic nature of such records reduces their applicability over large spatial regions, making it difficult to achieve the broad and detailed coverage needed to resolve the spatiotemporal complexity of SA hydroclimatic variability. We address these limitations by bringing together a network of observational climate data and tree ring records to develop the South American Drought Atlas (SADA), a spatiotemporal reconstruction of austral summer hydroclimate between 12° and 56°S latitude in SA, which allows us to characterize the spatiotemporal variability of extreme droughts and pluvials over the last 600 y. We also use the spatial covariance between the SADA and the Australian New Zealand Drought Atlas (ANZDA) (20) to identify and reconstruct the spatial fingerprints of the major climate drivers affecting hydroclimate variations over the SADA–ANZDA domain, which we then use to help diagnose the coupled ENSO/SAM events as drivers of extreme droughts and pluvials over the last half millennium in SA.

## Results

The SADA is a tree ring-based spatiotemporal reconstruction of austral summer (December, January, February [DJF]) droughts and pluvials over a large portion of SA (12° to 56°S) spanning the last 600 y. The reconstruction has been produced on a 2,715 point regular latitude–longitude grid with 0.5° resolution (Fig. 1*A*), and overall reflects contemporaneous summer soil moisture conditions, as well as those accumulated over previous seasons. The spatial extent and duration of the SADA make it the most spatially complete, highest-resolution, annually-resolved hydroclimate reconstruction that has specifically targeted SA.

The 286 tree ring chronology network used for reconstruction is shown in Fig. 1*A*. Compared to the self-calibrated Palmer Drought Severity Index (scPDSI) grid, its coverage is not spatially uniform across SA, mainly due to the dearth of long-lived trees in lowlands and deserts, the lack of suitable species for dendrochronology, and/or the absence of chronologies from species with dendrochronological potential. Despite these limitations, a well-calibrated and validated reconstruction of DJF scPDSI has been produced using an ensemble-based modification of the point-by-point regression (PPR) method applied in previous drought atlases (20–23) (*SI Appendix*, sections 5 and 7 and Fig. S5).

The instrumental scPDSI data cover the 1901 to 2015 period (*SI Appendix*, section 2). In contrast, the tree ring chronologies have a common end year of 2000 because of the wide variation in the dates of tree ring sampling. The 1901 to 1950 scPDSI data are of weaker quality, relative to data after 1951, due to the declining number of precipitation records available for the scPDSI grid (*SI Appendix*, Figs. S1 and S2). For this reason, the selected period for the reconstruction models was 1951 to 2000 because it is based on the best quality instrumental data. The most common method used in dendroclimatology to validate a reconstruction is to compare the tree ring climate estimates with instrumental data not included in the calibration. Given the relatively short instrumental period used for calibration (1951 to 2000) and the declining number of the instrumental series used in the scPDSI grid prior to 1951 (*SI Appendix*, Fig. S1), the reconstructions were primarily validated using a leave-one-out cross-validation procedure (24, 25) (*SI Appendix*, section 6, Fig. 1*B*, and *SI Appendix*, Fig. S4 *A–C*). The fraction of variance explained by regression in the calibration period (CRSQ [1951 to 2000]) is above 20% for almost the entire SADA domain and above 40% for more than 35% of the domain (Fig. 1*B*). The cross-validation reduction of error (CVRE) similarly indicates that over 20% of the variance is explained by the tree ring data in more than 75% of SADA domain (Fig. 1*C*).

Validation results are similar to those recorded for other drought atlases, such as the European Old World Drought Atlas (23), and suggest that the overall SADA is skillful. To further validate the SADA results, however, we compare our reconstructions to independent multicentury historical archives (18) in three different regions of SA: the Altiplano, central Chile, and the La Plata basin (*SI Appendix*, section 8 and Fig. S6). For this purpose, a superposed epoch analysis (SEA) was conducted (*Materials and Methods*), showing significant below/above scPDSI values are associated with the dry/wet extreme years reconstructed by documentary data for the three regions (Fig. 1 *D–F*). The highly significant phasing between the entirely independent scPDSI reconstruction and historical records add considerable confidence to both proxies as reliable sources of information for past hydroclimate variations across SA during past centuries.

**Temporal Patterns of Extreme Events.** There is considerable year-to-year variability in the estimates of the wet/dry conditions across the SADA domain (Fig. 2 *A* and *B*), while the average scPDSI for all 2,715 grid cells shows large decadal to centennial variability; the SADA domain has moved between wetter (e.g., early 19th century) and drier (e.g., mid-18th century) climates repeatedly over the past 600 y (Fig. 2*B*).

A temporally varying return-time analysis of the spatial extent of severe droughts/pluvials (scPDSI less than −2/greater than +2, respectively) reveals the frequency of widespread severe droughts over the past six centuries was nonstationary (Fig. 2*C*). There has been a steady increase in the frequency of widespread droughts since about 1930, with the highest frequency (one event per ∼10 y) since the 1960s, while the return time of severe widespread pluvials has remained relatively steady at 16 to 34 y over the period of study (Fig. 2*C*). A return time analysis of the spatial extent of both droughts and pluvials identifies the highest frequency of severe widespread events every ∼5 y post-1960, slightly higher than the second most frequent return period (∼6 y) recorded during the 17th century (gray line in Fig. 2*C*). A return time analysis of the average scPDSI value for the whole SADA domain (Fig. 2*D*) estimates that extreme pluvial events ocurrence were the most frequent since the second half of 20th century (one event per ∼11 y). The recurrence interval of extreme drought during the second half of the 20th century was short (∼12 y) but not different from the previous 17th-century period (∼13 y). Combining the occurrence of extreme droughts and pluvials, the shortest return time corresponds to the second half of the 20th century with one extreme event every ∼4.5 y, while the second shortest rate was recorded during the 17th century (one event per 5.5 y). Both analyses collectively indicate that widespread severe droughts and extreme pluvials over the SADA domain have been more frequent during the second half of the 20th century, relative to the rest of the SADA period.

**Hydroclimate Extremes and Societal Impacts.** Four well-documented extreme hydroclimatic events from three different regions are characterized by historical information completely independent of the SADA; note that the complete historical hydroclimatic reconstructions were compared in Fig. 1 *D–F* and *SI Appendix*, Fig. S6 (*SI*

*Appendix*, section 8). The silver mine drought (1800 to 1804) was the most severe 5-y drought recorded by Spaniards over more than 200 y of intensive mining in Potosí, Bolivia (26). Because water channels were used to power the silver mills in Potosí, the occurrence of wet and dry spring–summer seasons were consistently recorded between 1585 and 1807. SADA maps for the years 1800 to 1804 are consistent with the recorded historical drought and show severe dry conditions throughout the Altiplano (red square in Fig. 3*A*) that also extend into northwest and central Argentina (Fig. 3*A*). In both the SADA and historical data, the severity of the drought decreased in 1802 and intensified again in the following 2 y (Fig. 3*A*).

Historical records describe 1863 as the year of "complete and calamitous sterility" in central Chile (27). The great drought of 1863, which extended as far south as 40°S, allowed settlers in the extremely humid localities of Puerto Varas and Puerto Montt to burn and clear 30,000 ha of ancient rainforests. In this process of land clearance for agriculture, the oldest specimens in the region were burned (28). The 1863 SADA map (Fig. 3*B*) shows extremely dry conditions in central Chile and northern Chilean Patagonia that persisted for the following 3 y (Fig. 3*B*).

The subtropical region of the La Plata basin is frequently exposed to flood disasters. Cities and villages along the river margins such as the city of Santa Fe (mid-Paraná River basin, Argentina) have provided abundant documentary evidence of significant flood events. Based on this information, Prieto (29) reconstructed 38 large flood events between 1585 and 1815. We highlight here the 1651 to 1652 and 1723 floods. The floods of 1651 to 1652 destroyed more than half of the city of Santa Fe, leading to the relocation to its current position (29). Consistent with this event, the 1651 SADA map (Fig. 3*C*) shows very wet conditions throughout the La Plata basin, gradually decreasing toward the Chaco region in Argentina, southern Brazil, and Patagonia. In 1723, the villages and cultivated fields near the Paraná River suffered severe flooding, causing damage to buildings, diseases (e.g., dysentery), and loss of crops and livestock (29). The SADA map for the year 1723 shows extreme wet conditions for the upper Paraná basin (eastern Paraguay, southern Brazil, northeastern Argentina; Fig. 3*C*). These wet conditions also extend to the Pampas and central-western Argentina and gradually decrease toward central Chile. Our selected cases demonstrate that the SADA provides reliable spatiotemporal information on hydroclimate extremes and their connections with socioeconomic impacts across much of SA.

**Patterns of Hydroclimate Variability and the Influence of ENSO and SAM.** We used maximum covariance analysis (MCA) (30) to isolate patterns with common temporal variability between large-scale ocean–atmosphere climate modes and reconstructed scPDSI fields from the SADA and ANZDA. MCA identifies a coupled pattern explaining 48% of the total cross-covariance between scPDSI and austral summer (DJF) sea surface temperatures (HadISST dataset; *SI Appendix*, section 10, and Fig. 4*A*) over the period 1901 to 2000. The spatial loadings show an ENSO-like spatial pattern, where positive (negative) DJF SSTs in the tropical Pacific are coupled with wet (dry) conditions in southeastern SA (SESA), central Chile, and New Zealand. Dry (wet) conditions were also indicated in the Altiplano and central-east Australia during positive (negative) DJF SSTs. The correlation coefficients between the DJF SSTs for the Niño 3.4 sector (HadISST_N3.4; *SI Appendix*, section 10) and the scPDSI leading mode and SST leading modes are 0.63 (Fig. 4*C*) and 0.94, respectively. A similar spatial pattern emerges by applying MCA to instrumental SSTs and scPDSI datasets (*SI Appendix*, Fig. S8*A*) with a leading mode of coupled variability explaining 57% of the total covariance.

The MCA was repeated using DJF geopotential height at 500 mb (GPH500; *SI Appendix*, section 10) and reconstructed DJF

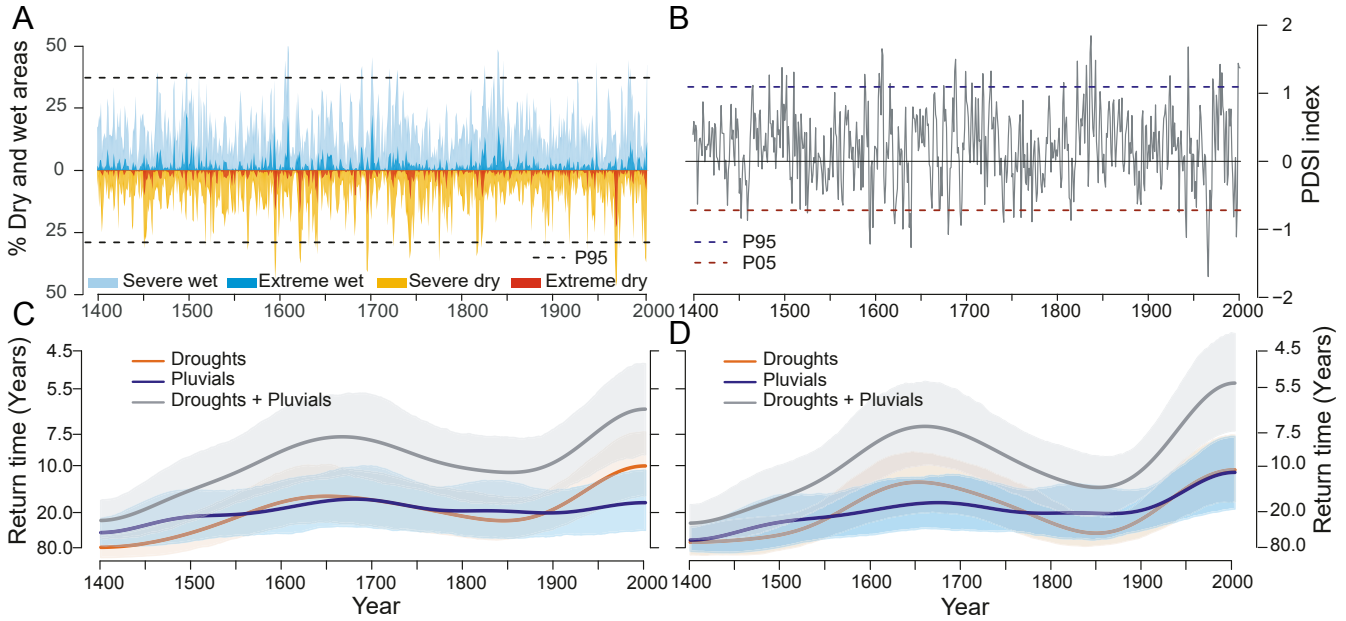


**Fig. 2.** Spatial magnitude and frequency of extreme drought and pluvial events in the SADA domain. (*A*) Percentage of area under severely dry (scPDSI −2, orange) and extremely dry (scPDSI −4, red) conditions, and for severely wet (scPDSI +2, light blue) and extremely wet (scPDSI +4, blue) conditions. The black short dashed lines indicate 95% percentiles of the distribution, from which severe widespread dry/wet events were selected for the return time analysis in *C*. (*B*) Average of SADA reconstructions over the entire study domain. The red and blue short dashed lines indicate the 5% and 95% percentiles of the distribution, respectively, from which extreme drought/wet events were selected for the return time analysis in *D*. (*C* and *D*) Time-varying frequency of the occurrences of severe widespread dry/wet scPDSI events and extreme dry/wet scPDSI events, respectively, between 1400 and 2000. A kernel smoothing method was used with a bandwidth of 50 y (49). The shaded areas (gray, blue, and orange) represent 95% confidence intervals based on 1,000 bootstrap simulations.

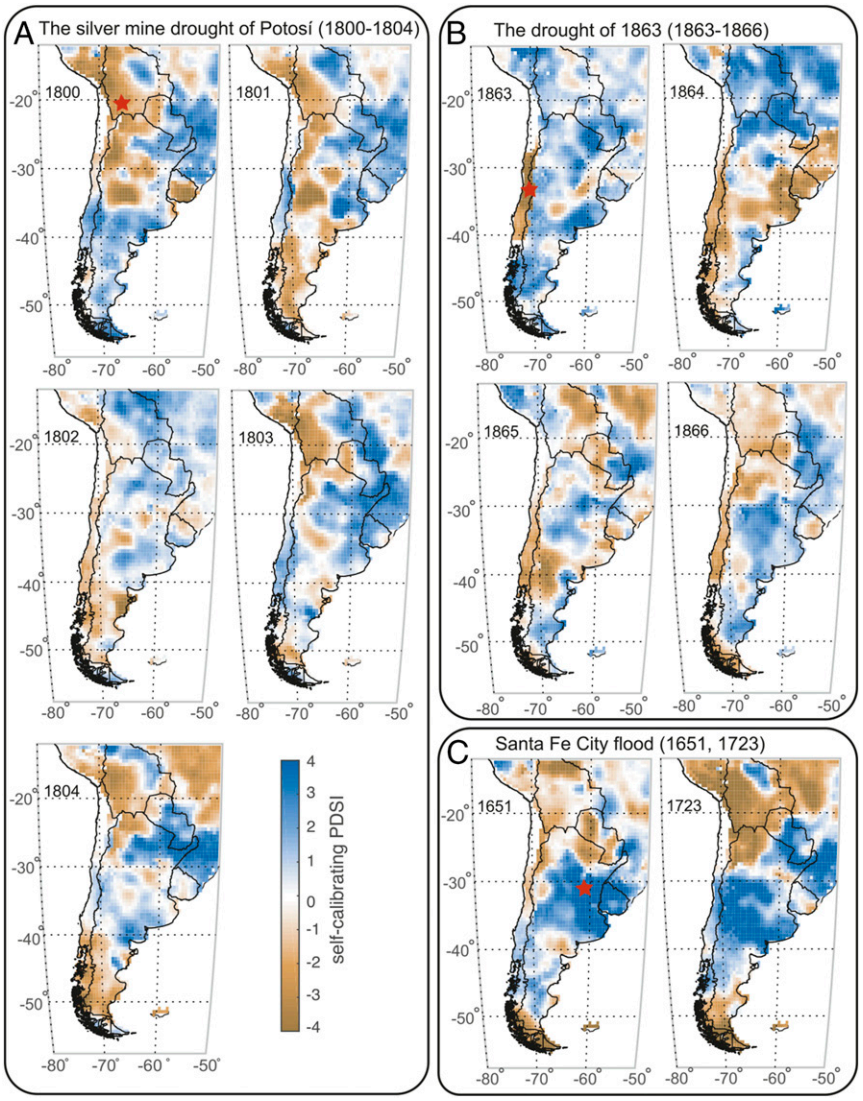


**Fig. 3.** Austral summer scPDSI maps of historical extremely dry/wet events in three regions from the SADA domain. (*A*) The silver mine drought of Potosí, Bolivia (1800 to 1804). (*B*) The central Chile drought of 1863 (1863 to 1866). (*C*) Santa Fe city floods (1651, 1723). The red stars indicate the geographic location of these recorded historical events.

scPDSI from SADA and ANZDA over the period 1948 to 2000. The resulting coupled spatiotemporal pattern accounts for 32% of the total cross-covariance and is consistent with the SAM (10) spatial pattern. The SAM, which is the primary mode of tropospheric circulation variability south of 20°S (31), was correlated with the first covariance-leading mode (scPDSI, $r = 0.55$; Fig. 4*D*; GPH500, $r = 0.67$). Variations in the SAM phases result from atmospheric mass exchanges between the sub-Antarctic (50 to 60°S) and mid-latitudes (40 to 50°S) in the SH. The positive phase is associated with decreased geopotential heights over Antarctica and strengthened and more poleward SH westerlies. Consequently, drier conditions occur in central Chile, Patagonia, New Zealand, and Tasmania during the positive phase (Fig. 4*B*). During the negative phase, opposite conditions are observed. Similar patterns emerged when MCA was applied to the instrumental GPH500 and scPDSI datasets, showing 28% of shared covariance between these fields (*SI Appendix*, Fig. S8*B*). The leading modes of covariance were extended over the common 1500 to 2000 period between SADA and ANZDA, and used as estimators of past ENSO and SAM variability in the SH domain, hereafter called ENSO-e and SAM-e, respectively (Fig. 4 *C* and *D*). The relationships between different paleoclimate ENSO and SAM reconstructions and our 500-y ENSO-e and SAM-e estimates are shown in *SI Appendix*, Figs. S9 and S10; correlations between the reconstructions are statistically significant in most cases.

The ENSO-e and SAM-e time series are negatively correlated ($r = -0.60$; $P < 0.0001$) over CE 1500 to 2000, providing a first indication of persistent interactions between ENSO and SAM over the past 500 y in the sense that La Niña causes a poleward shift of the westerlies and, hence, a positive SAM. To explore the influence of combinations of ENSO/SAM modes over the SA hydroclimate during the past 500 y, we examined those years when ENSO-e was negative and SAM-e was positive, and vice versa. A total of 25 (26) events for each phase was identified showing negative (positive) ENSO-e and positive (negative) SAM-e coefficients. The SADA composite map for the 25 coupled negative ENSO-e/positive SAM-e years (Fig. 4*E*) shows dominant dry conditions over central Chile, Patagonia, and southeast SA, whereas the Altiplano and northwestern Argentina are wet. The 26-y composite scPDSI map for positive ENSO-e/negative SAM-e years shows wet conditions across most

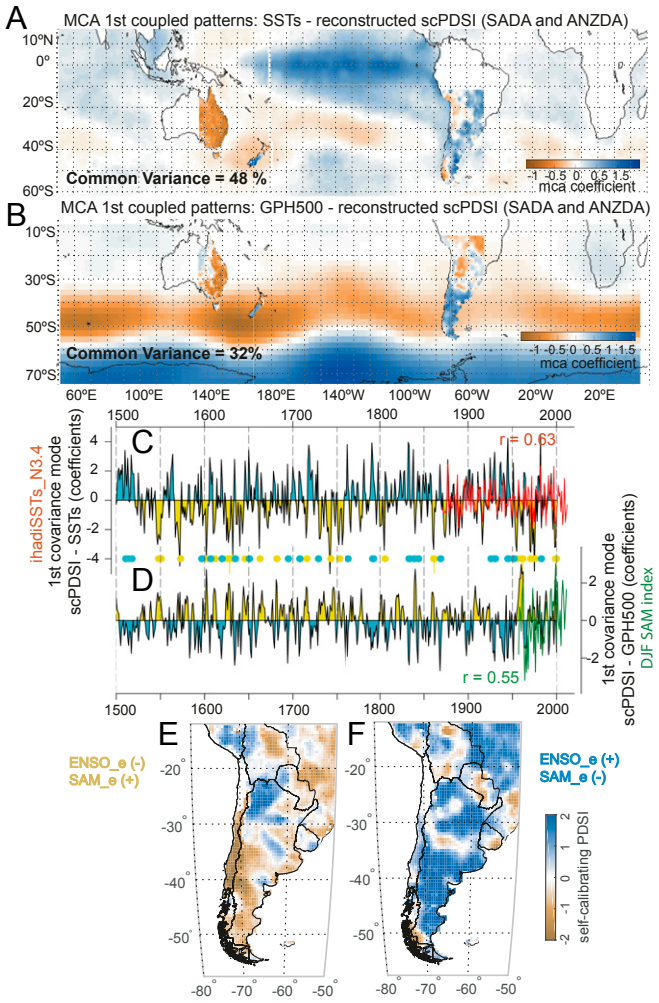


**Fig. 4.** Major SH forcing of hydroclimate variability and impacts on SADA composite maps. (*A*) Coupled spatial patterns of the leading MCA mode between SADA–ANZDA scPDSI and austral summer SSTs over the common period 1901 to 2000. (*B*) Coupled spatial patterns of the leading MCA mode between SADA–ANZDA scPDSI and austral summer geopotential height (500 hpa) over the common period 1948 to 2015. Temporal variability of the scPDSI leading modes for (*C*) ENSO and (*D*) SAM, resulting from the MCA analysis of *A* and *B*. Pearson's correlation coefficients (*r*) between the ENSO-e and SAM-e modes (black lines) and the DJF_NINO3.4 (red line) and SAM_DJF (green line) indices are given in red and green text in *C* and *D*, respectively. The yellow (light blue) dots indicate simultaneously anomalous negative (positive) ENSO-e and positive (negative) SAM-e index values from the MCA estimates. Composite SADA maps of the (*E*) 25 events of simultaneously anomalous negative ENSO-e and positive SAM-e years, and the (*F*) 26 events of simultaneously anomalous positive ENSO-e and negative SAM-e years.

of the SADA domain (Fig. 4*F*). The MCA analysis therefore provides evidence that persistent "in-phase" (in terms of impacts on the westerlies) ENSO/SAM anomalies explain most extended past droughts and pluvials across the SADA domain from CE 1500 to 2000 (SADA–ANZDA common period).

## Discussion

The SADA provides a long-term context for our present understanding of hydroclimate extremes in SA and identifies an intensification of the most widespread severe droughts since the mid-20th century (Fig. 2 *A* and *C*). This increase in extended droughts is consistent with the positive trend documented in the SAM during recent decades and the consequent poleward shift of the westerlies and associated storm tracks, leading to drier conditions in temperate southern SA (32, 33). Additionally, the western subtropics are becoming drier in response to the poleward expansion of the descending branch of the Hadley cell and the consequent southern extension of the dry subtropical belts (34). Concurrent with the intensification of widespread severe droughts, the SADA shows that extreme pluvials were also more frequent during the second half of the 20th century (Fig. 2 *B* and *D*). The increase in extreme wet events is largely concentrated in the wet SESA (*SI Appendix*, Fig. S7 *C* and *G*). Positive rainfall trends were recorded in subtropical central-southeastern SA and a parallel increase in the magnitude and frequency of extreme wet events since the 1950s (35, 36). Precipitation in this region is expected to increase under global warming scenarios (37) inducing a southward displacement of both the South Atlantic Convergence Zone and the Atlantic subtropical high (38). Additionally, future projections indicate an intensification of the low-level jet in SA, causing a wetting in SESA (39). However, the wetting trend over SESA and the poleward shift of the westerlies in summer are also modulated by ozone depletion over Antarctica, and its projected recovery may revert these trends during this century (10, 36).

The SADA was developed using the same method of climate field reconstruction used to produce six other independent drought atlases, five in the Northern Hemisphere and the ANZDA in the SH. The simultaneous use of the SADA and ANZDA allow us to determine the influence of tropical–extratropical interactions on hydroclimate variability in the Pacific domain of the SH over the past several centuries. Using MCA (Fig. 4), we isolated the coupled patterns of maximum-shared covariance between reconstructed scPDSI from SADA and ANZDA, with hemispheric SST and pressure field variations. Both reconstructed and instrumental fields show important fractions of the total explained covariance related to ENSO-like (48%) and SAM-like (32%) spatial patterns. Taken together, these coupled spatiotemporal patterns suggest that ENSO and SAM largely explain most of the interannual scPDSI variability in the SADA and ANZDA domains. Our results highlight that the combined impacts between negative (positive) ENSO and positive (negative) SAM events have modulated the occurrence of severe drought/pluvial conditions in large areas of SA during the last 500 y. Modeling will be required to determine whether these extreme events arise from ENSO forcing of the SAM combined with constructive internal SAM variability. In a long-term context, the unprecedented persistent positive SAM trend in the last five decades, coupled with the poleward migration of the westerlies, has largely contributed to the persistent drying trends in southwestern SA (32, 33). Because persistent positive SAM conditions are expected to continue for decades (38), even though rising greenhouse gases and ozone recovery may induce opposite trends (10), it is particularly important to advance our knowledge on the ENSO–SAM interactions under global warming in the 21st century. Here, we demonstrate how the SADA provides critical hydroclimatic information that can be used to validate last millennium simulations and consequently assess whether models realistically represent future tropical–extratropical interactions and their synergistic impacts on SA hydroclimatic variability. The use of the SADA in combination with other drought atlases and global climate field reconstruction products, such as the Paleo Hydrodynamics Data Assimilation (40) and the Last Millennium Reanalysis (41), therefore promises to improve our understanding of SH hydroclimate variability and change on interannual to centennial timescales and therefore refine our ability to project near-future changes due to continued emission of greenhouse gases into the atmosphere.

## Materials and Methods

**Observational Climate and Tree Ring Data.** The observational data used to compute instrumental scPDSI was an ensemble of the interpolated fields of

monthly climate observations from three datasets: 1) precipitation, temperature, and potential evapotranspiration data from the Climatic Research Unit Time Series (CRU) TS 4.01 (42), enhanced by the incorporation of precipitation and temperature records from the Argentinean Institute of Snow, Ice and Environmental Research (IANIGLA-CONICET) database (*SI Appendix*, section 1 and Fig. S1); 2) precipitation and air temperature dataset from the University of Delaware (43); and 3) the precipitation dataset from Global Precipitation Climatology Centre (44). The computed monthly scPDSI data were seasonalized to develop average data for the austral summer season (DJF). The DJF scPDSI reflects spring–summer soil moisture conditions from 2,715 grid cells (0.5° longitude by 0.5° latitude) covering the study domain (12° to 56°S; 50° to 80°W) (*SI Appendix*, section 2).

During the last several decades, tree ring scientists from Chile, Argentina, and Bolivia have vastly increased tree ring sample collections in SA (17). The SADA includes data from 286 tree ring chronologies (*SI Appendix*, section 3 and Table S1), mainly concentrated on both sides of the Andes Cordillera (16° to 56°S), from the Altiplano and intermontane subtropical valleys to the Patagonian forests at the southern tip of the continent (Fig. 1*A*). Additionally, new collections from tropical lowlands have allowed extension of the geographical coverage of tree ring records to lower latitudes. The target period (CE 1400 to 2000) for reconstruction of scPDSI is the consequence of a relatively high number of longer tree ring chronologies and good spatial coverage along the Andes (*SI Appendix*, Fig. S3). To preserve medium frequency variability due to climate, the 286 tree ring chronologies were standardized using "signal-free" methods (45) (*SI Appendix*, section 4).

**Reconstruction Method.** A modification of the well-tested nested PPR method (22) was used to produce the SADA (*SI Appendix*, section 5). The version presented here is an average derived from an ensemble approach using 15-ensemble members, where each member uses a different search radius (200-, 500-, 800-, 1,100-, and 1,500-km distance) to locate the tree ring chronologies for reconstructing scPDSI at each grid point based on a weighted power correlation ($P = 0$; $P = 1$; $P = 2$) between tree ring chronologies and scPDSI (23). The 15 output model members were averaged, recalibrated, and revalidated directly against instrumental data. The average correlation between ensemble members at each grid point was then calculated. Because opposite precipitation trends occur on both side of the highest Andes region (24° to 38°S), we produce two independent 15-member ensemble reconstructions on each sides of the Andes that were merged to create a final reconstruction.

**Comparison between Historical and Tree Ring-Based Hydroclimate Reconstructions.** SEA, a nonparametric statistical technique, was used to determine the relationships between the regional scPDSI reconstructions and drought/pluvial events from climate reconstructions based on historical records. The selected scPDSI regions (red rectangles in Fig. 1*A*) for these analyses were the Altiplano (17° to 23°S; 66° to 70°W), central Chile (30° to 37°S; 70° to 72°W), and part of La Plata basin (31° to 37°S; 56° to 61°W). The historical sources are precipitation records from Potosí, Bolivia (Altiplano; ref. 21), the snow and drought records from the Andes region of central Chile (ref. 46 and sources references therein), and the flood records in the city of Santa Fe (mid-Paraná river, La Plata basin; ref. 29). In this analysis, the regional scPDSI records were used as the background time series and the dates of dry/wet years in the historical series as event years (Dataset S1). For each event, a 9-y lag window was used with the event year as the central value plus 4 y before and after the event. The 9-y scPDSI data were averaged for each event to produce a mean pattern related to the historical event. The mean scPDSI pattern for the selected years was statistically evaluated for significance (95% confidence interval) by performing 1,000 Monte Carlo simulations (47) using random years from the scPDSI record.

**Analysis of Hydrological Extreme Events.** Dry/wet events were characterized by their intensity and spatial extent. We calculated the average of scPDSI for the entire SADA domain from CE 1400 to 2000. Extreme intensity dry/pluvial events were determined by including scPDSI values lower/higher than the 95th and 5th percentiles, respectively. To determine large spatially widespread dry/wet events, we first calculated the interannual fluctuations in the percent area of severe dry/wet conditions, i.e., the total number of grid points with scPDSI values less than −2 for severe dry and greater than 2 for severe wet years. Those severe dry/wet events that exceeded the 95th percentile of spatial extent were considered extreme spatially widespread pluvial/drought events. Temporary changes in the occurrence-rate estimation of extremes in intensity and spatial extent of drought/pluvial events were estimated using the nonparametric kernel function. This technique allows the detection of nonmonotonic trends without imposing parametric restrictions. For this purpose, a Gaussian kernel function was applied in order to estimate the probability of occurrence of one specific extreme event using a 60-y bandwidth. To better interpret these estimates, confidence bands at the 95% level were obtained using 1,000 bootstrap simulations (48, 49).

**MCA for Reconstructed scPDSI and Climate Modes.** To describe how SST and geopotential height (500 mb) (*SI Appendix*, section 10, for dataset reference) covary with the summer scPDSI from the SADA and the ANZDA, we used MCA. This method is widely used in climate research and identifies coupled patterns in two data fields that share the maximum amount of covariance (50). This statistical tool identifies the common signal while separating stochastic noise from other factors. The leading modes obtained by MCA were used as estimators of ENSO (ENSO-e) and SAM (SAM-e) variability for the past 500 y (Dataset S2). The resulting time series of the difference between both climate index estimators was used to determine the anomalous negative/positive values by the 5th and 95th percentiles, respectively (Dataset S3). The 25 (26) negative (positive) values were associated with coupled anomalous negative (positive) ENSO-e and positive (negative) SAM-e events.

**Data Deposition.** Tree ring chronologies, instrumental and reconstructed scPDSI (SADA) are available at the Center for Climate and Resilience Research $(CR)^2$, http://www.cr2.cl/datos-dendro-sada/ (51). Historical hydroclimate reconstructions together with regional scPDSI used to validate each proxy are presented in Dataset S1. The main leading modes used as estimators of ENSO and SAM variability for the past 500 y together with the 25 (26) negative (positive) coupled ENSO/SAM events are also presented in Datasets S2 and S3. Additional instrumental climate data used in the paper are available in the corresponding hosting websites.

**ACKNOWLEDGMENTS.** We acknowledge the Servicio Meteorológico Nacional, Instituto Nacional de Tecnología Agropecuaria, Secretaría de Recursos Hídricos, Autoridad Interjurisdiccional de Cuencas, Dirección Provincial del Agua in Argentina, Administracion de Parques Nacionales Argentina, Estancia Los Huemules, Dirección General de Aguas and Dirección Meteorológica de Chile in Chile, and Servicio Nacional de Meterología e Hidrología in Bolivia and Perú for providing quality-controlled daily and monthly climate data, which were essential for developing the reconstruction models. This study was supported by the Agencia Nacional de Promoción Científica y Tecnológica, Argentina (PICT 2013-1880), Consejo Nacional de Investigaciones Científicas y Tecnológicas (PIP 11220130100584) projects. The Inter-American Institute for Global Change Research CRN03, CRN2047 and CRN027 funded part of this study through grants (NSF Grant GEO-0452325). M.S.M., M.E.F., and R.V. received partial support from Fondo Nacional de Desarrollo Científico, Tecnológico y de Innovación Tecnológica, Perú (FONDECYT-BM-INC.INV 039-2019); M.S.M. was supported in part by National Science Foundation Grant AGS-1702789. M.S.M., R.V., A.M.S., I.A.M., D.A.C., A.L., R.U.-J., and C.L. were supported in part by the THEMES project funded by the BNP Paribas Foundation in the frame of its "Climate Initiative" program. J.E.S., E.R.C., and A.P.W. were supported in part by NSF Grant AGS-1602581; M.S.M., R.V., M.E.F., J.E.S., and A.P.W. were supported in part by NSF Grant OISE-1743738; J.E.S. was supported in part by NSF Grant AGS-1805490. LDEO contribution #8418. V.M. was supported in part by the Russian State Assignment Project 0148-2019-0004. D.A.C., J.B., C.L., A.G.-R., A.A.M., M.R.-B., C.A., G.V., D.A., and I.A.-B. were supported by the Chilean Research Council (FONDECYT 1161381, 1201411, 1181956, and 11161061). D.A.C., A.L., A.G.-R., R.U.-J., and A.A.M. were supported by the National Agency for Research and Development Chile (ANID/FONDAP/15110009). A.G.-R. was supported by the National Agency for Research and Development Chile (ANID/PAI/77190101). M.E.F. was supported in part by ANPCyT PICT 2014-2797. R.U.-J. was partially supported by PAI/ANID/7818I20003. A.L., J.B., and R.U.-J. were supported in part by the Fondecyt Grant 1171496.

1. M. R. Prieto *et al*., "Sequías extremas en Mendoza durante el siglo XX y principios del XXI. Administración de la carencia y conflictos socio-políticos" in *Medio Ambiente y Transformación Rural en la Argentina Contemporánea*, G. Zarrilli, M. Ruffini, Eds. (Universidad Nacional de Quilmes, Buenos Aires, 2020), pp. 1–30.
2. J. A. Arrese, "16th Session of the Commission on Sustainable Development" (United Nations, New York, 2008).
3. R. D. Garreaud *et al*., The 2010–2015 megadrought in central Chile: Impacts on regional hydroclimate and vegetation. *Hydrol. Earth Syst. Sci.* **21**, 6307–6327 (2017).
4. R. Neukom *et al*., Facing unprecedented drying of the Central Andes? Precipitation variability over the period AD 1000–2100. *Environ. Res. Lett.* **10**, 84017 (2015).
5. C. Vera *et al*., Toward a unified view of the American monsoon systems. *J. Clim.* **19**, 4977–5000 (2006).

6. R. D. Garreaud, M. Vuille, R. Compagnucci, J. Marengo, Present day South American climate. *Palaeogeogr. Palaeoclim. Palaeocl.* **281**, 180–195 (2009).
7. R. Seager *et al*., Tropical oceanic causes of interannual to multidecadal precipitation variability in southeast South America over the past century. *J. Clim.* **23**, 5517–5539 (2010).
8. C. Deser, M. A. Alexander, S.-P. Xie, A. S. Phillips, Sea surface temperature variability: Patterns and mechanisms. *Annu. Rev. Mar. Sci.* **2**, 115–143 (2010).
9. M. J. McPhaden, S. E. Zebiak, M. H. Glantz, ENSO as an integrating concept in earth science. *Science* **314**, 1740–1745 (2006).
10. G. J. Marshall, Trends in the southern annular mode from observations and reanalyses. *J. Clim.* **16**, 4134–4143 (2003).
11. L. M. Polvani, M. Previdi, C. Deser, Large cancellation, due to ozone recovery, of future Southern Hemisphere atmospheric circulation trends. *Geophys. Res. Lett.* **38**, L04707 (2011).
12. R. D. Garreaud *et al*., The Central Chile mega drought (2010–2018): A climate dynamics perspective. *Int. J. Climatol.* **40**, 421–439 (2019).
13. C. Lucas, B. Timbal, H. Nguyen, The expanding tropics: A critical assessment of the observational and modeling studies. *Wiley Interdiscip. Rev. Clim. Change* **5**, 89–112 (2014).
14. R. Seager *et al*., Climate variability and change in Mediterranean-type climate regions. *J. Clim.* **32**, 2887–2916 (2019).
15. M. L. L'Heureux, D. W. J. Thompson, Observed relationship between the El Niño–Southern Oscillation and the extratropical zonal-mean circulation. *J. Clim.* **19**, 276–287 (2006).
16. X. Yuan, M. R. Kaplan, M. A. Cane, The interconnected global climate system—a review of tropical-polar teleconnections. *J. Clim.* **31**, 5765–5792 (2018).
17. J. A. Boninsegna *et al*., Dendroclimatological reconstructions in South America: A review. *Palaeogeogr. Palaeoclimatol. Palaeoecol.* **281**, 210–228 (2009).
18. M. R. Prieto, R. Garcia-Herrera, Documentary sources from South America: Potential for climate reconstruction. *Palaeogeogr. Palaeoclimatol. Palaeoecol.* **281**, 196–209 (2009).
19. M. Vuille *et al*., A review of the South American monsoon history as recorded in stable isotopic proxies over the past two millennia. *Clim. Past* **8**, 1309–1321 (2012).
20. J. G. Palmer *et al*., Drought variability in the eastern Australia and New Zealand summer drought atlas (ANZDA, CE 1500–2012) modulated by the Interdecadal Pacific Oscillation. *Environ. Res. Lett.* **10**, 124002 (2015).
21. E. R. Cook, C. A. Woodhouse, C. M. Eakin, D. M. Meko, D. W. Stahle, Long-term aridity changes in the western United States. *Science* **306**, 1015–1018 (2004).
22. E. R. Cook *et al*., Asian monsoon failure and megadrought during the last millennium. *Science* **328**, 486–489 (2010).
23. E. R. Cook *et al*., Old World megadroughts and pluvials during the Common Era. *Sci. Adv.* **1**, e1500561 (2015).
24. J. Michaelsen, Cross-validation in statistical climate forecast models. *J. Clim. Appl. Meteorol.* **26**, 1589–1600 (1987).
25. D. M. Meko, Dendroclimatic reconstruction with time varying subsets of tree indices. *J. Clim.* **10**, 687–696 (1997).
26. A. Gioda, M. R. Prieto, Histoire des sécheresses andines: Potosi El Niño et le Petit Age Glaciaire. *Meteorologie* **8**, 33–42 (1999).
27. B. Vicuña Mackenna, *Ensayo Histórico Sobre el Clima de Chile: Desde los Tiempos Prehistóricos Hasta el Gran Temporal de Julio de 1877*, (Imprenta del Mercurio, Valparaíso, Chile, 1877).
28. R. Elizalde Mac-Clure, *La Sobrevivencia de Chile. La Conservación de sus Recursos Naturales*, (Minis. Agr., S.A.G., Santiago, Chile, 1970).
29. M. R. Prieto, ENSO signals in South America: Rains and floods in the Parana River during colonial times. *Clim. Change* **83**, 39–54 (2007).
30. C. S. Bretherton, C. Smith, J. M. Wallace, An intercomparison of methods for finding coupled patterns in climate data. *J. Clim.* **5**, 541–560 (1992).
31. D. W. J. Thompson, J. M. Wallace, G. C. Hegerl, Annular modes in the extratropical circulation. Part II: Trends. *J. Clim.* **13**, 1018–1036 (2000).
32. N. P. Gillett, T. D. Kell, P. D. Jones, Regional climate impacts of the Southern Annular Mode. *Geophys. Res. Lett.* **33**, L23704 (2006).
33. R. Villalba *et al*., Unusual Southern Hemisphere tree growth patterns induced by changes in the Southern Annular Mode. *Nat. Geosci.* **5**, 793–798 (2012).
34. Y. Hu, Q. Fu, Observed poleward expansion of the Hadley circulation since 1979. *Atmos. Chem. Phys.* **7**, 5229–5236 (2007).
35. M. Re, V. R. Barros, Extreme rainfalls in SE South America. *Clim. Change* **96**, 119–136 (2009).
36. P. L. M. Gonzalez, L. Goddard, A. M. Greene, Twentieth-century summer precipitation in South Eastern South America: Comparison of gridded and station data. *Int. J. Climatol.* **33**, 2923–2928 (2013).
37. J. H. Christensen *et al*., ""Climate phenomena and their Relevance for future regional climate change"" in *Climate Change 2013: The Physical Science Basis. Contribution of Working Group I to the Fifth Assessment Report of the Intergovernmental Panel on Climate Change*, T. F. Stocker, Ed. (Cambridge University Press, Cambridge, UK, 2013), pp. 1217–1308.
38. J. M. Arblaster, G. A. Meehl, D. J. Karoly, Future climate change in the Southern Hemisphere: Competing effects of ozone and greenhouse gases. *Geophys. Res. Lett.* **38**, L02701 (2011).
39. A. Seth, M. Rojas, S. A. Rauscher, CMIP3 projected changes in the annual cycle of the South American Monsoon. *Clim. Change* **98**, 331–357 (2010).
40. N. J. Steiger, J. E. Smerdon, E. R. Cook, B. I. Cook, A reconstruction of global hydroclimate and dynamical variables over the Common Era. *Sci. Data* **5**, 180086 (2018).
41. R. Tardif *et al*., Last Millennium Reanalysis with an expanded proxy database and seasonal proxy modeling. *Clim. Past* **15**, 1251–1273 (2019).
42. I. Harris, P. D. Jones, T. J. Osborn, D. H. Lister, Updated high-resolution grids of monthly climatic observations—The CRU TS3.10 dataset. *Int. J. Climatol.* **34**, 623–642 (2014).
43. K. Matsuura, National Center for Atmospheric Research Staff, The Climate Data Guide: Global (land) Precipitation and Temperature: Willmott & Matsuura, University of Delaware. https://climatedataguide.ucar.edu/climate-data/global-land-precipitation-and-temperature-willmott-matsuura-university-delaware. Accessed 20 October 2017.
44. National Center for Atmospheric Research Staff, The Climate Data Guide: GPCC: Global Precipitation Climatology Centre. https://climatedataguide.ucar.edu/climate-data/gpcc-global-precipitation-climatology-centre. Accessed 20 September 2018.
45. T. Melvin, K. Briffa, A "signal-free" approach to dendroclimatic standardization. *Dendrochronologia* **26**, 71–86 (2008).
46. M. H. Masiokas *et al*., Snowpack variations since AD 1150 in the Andes of Chile and Argentina (30°–37°S) inferred from rainfall, tree-ring and documentary records. *J. Geophys. Res.* **117**, D05112 (2012).
47. C. Z. Mooney, R. D. Duval, *Bootstrapping: A Nonparametric Approach to Statistical Inference*, (Sage University Paper Series on Quantitative Applications in the Social Sciences, Sage University, Newbury Park, CA, 1993).
48. A. Cowling, P. Hall, M. J. Phillips, Bootstrap confidence regions for the intensity of a Poisson point process. *J. Am. Stat. Assoc.* **91**, 1516–1524 (1996).
49. M. Mudelsee, *Climate Time Series Analysis: Classical Statistical and Bootstrap Methods*, (Atmospheric and Oceanographic Sciences Library, Springer, 2014), Vol. 51.
50. D. Wilks, *Statistical Methods in the Atmospheric Sciences*, (Academic, 2011).
51. M. S. Morales *et al*, South American Drought Atlas (SADA) 1400-2000 C.E. http://www.cr2.cl/datos-dendro-sada/. Deposited 2 June 2020.